From breast cancer cell homing to the onset of early bone metastasis: dynamic bone (re)modeling as a driver of osteolytic disease

Sarah A. E. Young[1], Anna-Dorothea Heller[1], Daniela S. Garske[1], Maximilian Rummler[1,2], Victoria Qian[1], Agnes Ellinghaus[3], Georg N. Duda[3], Bettina M. Willie[2], Anika Grüneboom[4], Amaia Cipitria[1,5,6*]

[1] Department of Biomaterials, Max Planck Institute of Colloids and Interfaces, Potsdam, Germany

[2] Research Centre, Shriners Hospital for Children - Canada, Faculty of Dental Medicine and Oral Health Sciences, McGill University, Montreal, Canada

[3] Julius Wolff Institute, Berlin Institute of Health at Charité – Universitätsmedizin Berlin, Germany

[4] Leibniz-Institute for Advancing Analytics – ISAS – e.V., Dortmund, Germany

[5] Group of Bioengineering in Regeneration and Cancer, Biodonostia Health Research Institute, San Sebastian, Spain

[6] IKERBASQUE, Basque Foundation for Science, Bilbao, Spain

Corresponding author: amaia.cipitria@mpikg.mpg.de

Phone number: +49 331 567-9452

Max Planck Institute of Colloids and Interfaces, Am Mühlenberg 1, 14476 Potsdam

Abstract:

Breast cancer often metastasizes to bone and causes osteolytic lesions. Dynamic changes in the bone microenvironment are rarely studied but are hypothesized to influence the establishment and progression of bone metastatic lesions. Here, we developed an experimental bone metastasis mouse model to detect and characterize breast cancer cell homing and the onset of early bone metastasis. We studied the dissemination of cancer cells to (intact) bones, their proliferative state and direct microenvironment, using 3D light-sheet fluorescence microscopy (LSFM) and multiscale correlative tissue characterization. We show that cancer cells home in all bone compartments using intact bones, with a preference for small clusters in the bone marrow and larger clusters in the periosteum. We developed an image analysis tool to detect and track early bone osteolytic lesions, quantifying their onset, location and growth. Osteolytic lesions were only detected in the metaphysis and were classified as three different types depending on location. Surprisingly, we observed altered bone (re)modeling with increased new bone formation in animals without detectable osteolytic lesions. Our study suggests an early systemic effect of breast cancer cells in the bone microenvironment and provides novel insights of the structural and biophysical changes during the early phase of metastasis.

Keywords:

Breast cancer; Bone metastasis; Cancer cell homing; Dynamic bone (re)modeling; Early bone osteolytic lesion; 3D light-sheet fluorescence microscopy (LSFM); In vivo microcomputed tomography (microCT) time-lapse morphometry; Multiscale correlative tissue characterization

1. Introduction

Bone metastases often occur from breast cancer, one of the leading causes for cancer-associated deaths among women worldwide[1]. 65-80% of patients with advanced breast cancer develop bone metastasis[2,3]. In the bone it leads to osteolytic lesions[2] and drastically lowers the prognosis of survival[4]. The metastatic cancer undergoes different stages of activity, from a dormant invisible stage that can last up to decades, to active growing metastases that change the bone structure, up to overt metastasis and skeletal morbidity[5–7]. Much work has been reported on primary tumor growth and advanced overt metastasis, but less is known about the early phases of metastasis such as the premetastatic niche[8], the antimetastatic niche[9], the dormant niche[10] or the early metastasis[11].

The biophysical and structural properties of the tumor microenvironment have become a focus point in metastasis research. Advanced physical science techniques and quantification methods hold great potential to reveal physico-chemical alterations that modulate early phases of metastasis. A recent study showed that tumor-derived collagen type III sustained tumor cell dormancy, and changes in architecture and density restored proliferation [12]. Fibronectin fibers were found to be under lower tension in tumor invaded tissues compared to healthy tissue[13]. In the context of bone tissue, less-mature hydroxyapatite nanocrystals in the mineralized bone tissue were associated with the initiation of metastasis [11]. A following study, recapitulated the premetastatic niche by systemic injection of tumor conditioned media, which induced increased bone formation of altered quality[14] and suggested potential consequences on initial seeding of breast cancer cells. However, multimodal 3D imaging is required to shed light on the tight interlink of cancer biology and tissue structural changes during early stages of the disease. This is particularly challenging in the mineralized bone tissue, since it is less accessible than soft organs and imaging of soft tissue compartments within 3D intact bones requires advanced multimodal 3D imaging[15,16].

Bone is a highly dynamic organ and mineralized tissue is constantly (re)modelled[17]. The differences in bone turnover between young and older animals did not affect the seeding of breast cancer cells but it

influenced the development of overt osteolytic bone metastasis, as young mice with high bone turnover exhibited higher numbers of overt skeletal lesions, as quantified by histology and ex vivo microcomputed tomography (microCT)[18]. Another study used longitudinal *in vivo* microCT to study the dynamics of bone metastasis and quantify bulk bone destruction upon direct intratibial injection of cancer cells[19]. However, the spatial resolution of the *in vivo* microCT scans limited the quantitative analysis to large bone destruction during advanced overt metastasis. In this context, we recently revealed anatomical site-specific differences in bone (re)modeling of healthy 12-week-old skeletally mature mice and this served as baseline to detect the onset of early pathological events, taking breast cancer metastasis as proof-of-concept[20]. Understanding the dynamic changes in the bone microenvironment and correlating this with visualization and quantification of homing of breast cancer cells, may help shed light on the role of bone tissue dynamics on the seeding of cancer cells and/or on the initiation of osteolytic lesions.

We hypothesized that the dynamic microenvironment in the bone drives the progression of early bone metastasis. Therefore, we established an experimental bone metastasis mouse model to study the early stages of metastasis, from breast cancer cell homing to the onset of early bone lesions, both *in vivo* and *ex* vivo. Skeletally mature 12-week-old female BALB/c nude mice were injected intracardially with $eGFP^+$ breast cancer bone tropic cells, to recapitulate the stage of disseminated cancer cells in circulation. The homing of breast cancer cells and cell clusters to the bone marrow was studied with advanced light-sheet fluorescence microscopy (LSFM) using 3D (intact) bones. LSFM revealed breast cancer cells and small clusters disseminated to all bones and different compartments. (Re)modeling in the long bones was studied with the help of *in vivo* microCT-based time-lapse morphometry. The method was further adapted to detect cortical osteolytic lesions at an early time point, allowing the quantification of these lesions and revealing different types of lesions in both cortical and trabecular bone. In addition, we used advanced *ex vivo* methods to characterize the structural changes caused by early lesions using multimodal methods. The results suggest that dynamic bone (re)modeling is a driver of metastasis, with cancer cells reaching every bone compartment, yet lesions only occurring in dynamic regions like the metaphysis. Surprisingly,

the (re)modeling analysis also showed that enhanced mineralization is present in animals with systemic cancer cells in the absence of detectable osteolytic lesions.

2. Results

Breast cancer cells and small clusters homing in the bone marrow visualized by 3D light-sheet fluorescence microscopy

LSFM was used to study the homing of breast cancer cells and small cell clusters in 3D (intact) tibiae. Optical clearing makes the bone transparent to the LSFM and allows 3D visualization of fluorescently labeled ($eGFP^+$) breast cancer cells in the bone marrow and in the periosteum. The (virtual) 2D section overview image in Fig. 1A shows cancer cells and small cell clusters infiltrating the entire bone marrow of the tibia (Fig. 1A.1-2) (Supplementary Movie 1). In addition, larger and denser clusters of cancer cells were found in the periosteal region (Fig. 1A.3). Single cells and small clusters of only a few cells were found in between muscle fibers and all over the periosteal bone surface (Fig. 1A.4). The quantitative analysis of the size and spatial distribution of around 5,500 cells and cell clusters (Fig. 1C) shows, that most tumor cells are in close proximity to the cortical bone surface, with a mean distance of around 50 µm depicted in Fig. 1F and a mean diameter ranging between 31 – 36 µm Fig. 1D (Supplementary Movie 2). Periosteal cell clusters on the other hand can be much larger with volumes up to 0.1 mm^3 (Fig. 1E).

Further descriptive analysis of five different bones revealed that cancer cells and cell clusters are detected in various bone compartments like the diaphysis, metaphysis and epiphysis, as well as in different types of bone such as tibia and fibula, as shown in Fig. 2.

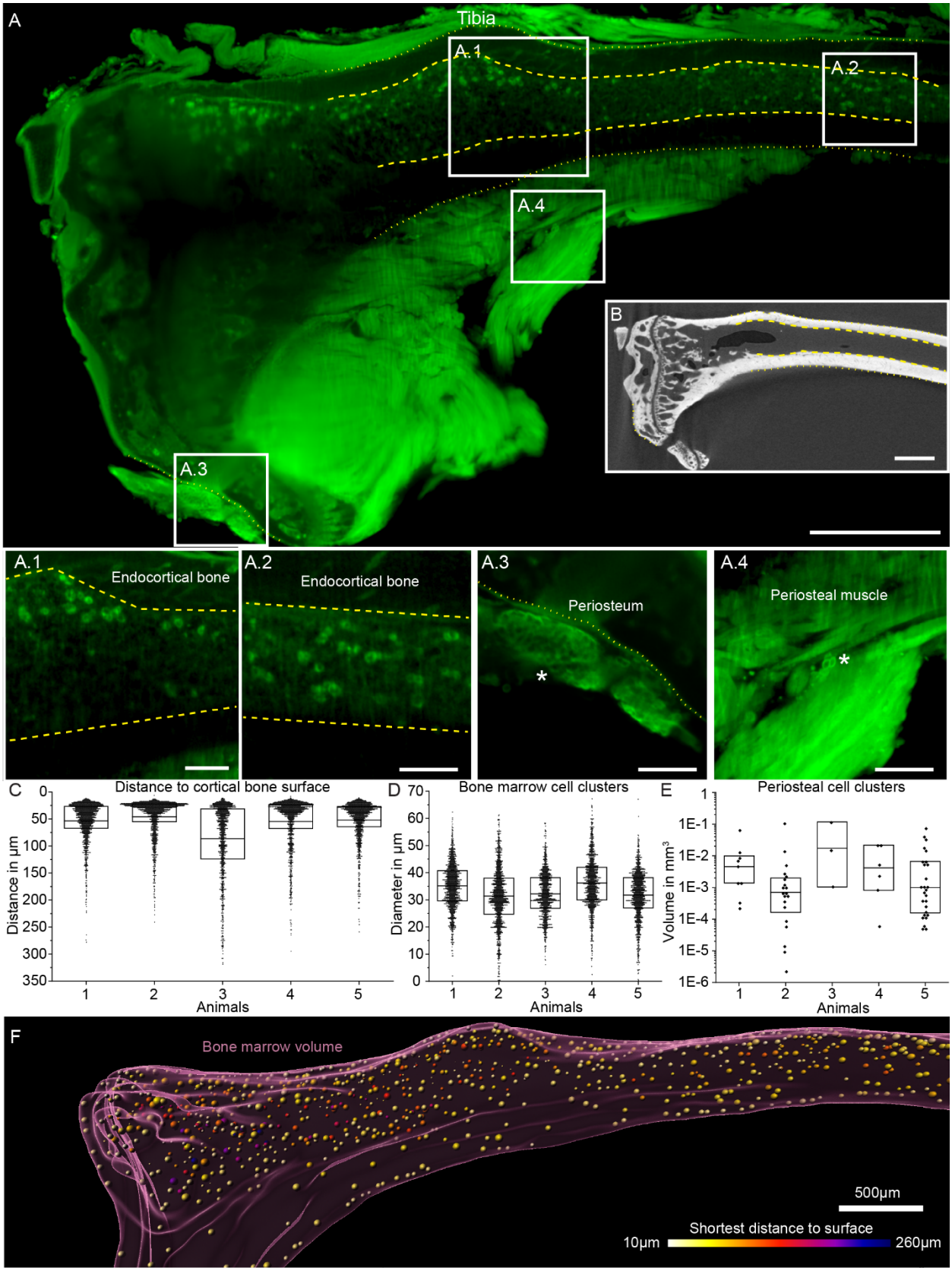
A
Tibia
A.1
A.2
A.3
A.4
B
A.1
Endocortical bone
A.2
Endocortical bone
A.3
Periosteum
A.4
Periosteal muscle
C
Distance to cortical bone surface
Distance in µm
Animals
D
Bone marrow cell clusters
Diameter in µm
Animals
E
Periosteal cell clusters
Volume in mm³
Animals
F
Bone marrow volume
500µm
Shortest distance to surface
10µm
260µm

Fig 1: Light-sheet fluorescence microscopy (LSFM) and 3D quantification of the spatial and size distribution of breast cancer cells and cell clusters homing in the bone microenvironment.

LSFM images of one (virtual) section are depicted for (**A**) one entire bone, with enlargements of small cell clusters in the bone marrow on the (**A.1**) upper diaphysis with highlighted endocortical bone surface, (**A.2**) lower diaphysis with highlighted endocortical bone surface, (**A.3**) periosteal site as large dense cluster (marked with an asterisk) and (**A.4**) in between muscle tissue as small clusters (marked with an asterisk). (**B**) MicroCT image of the same (virtual) bone section as shown in A, with highlighted endocortical and periosteal bone surfaces. Quantification of breast cancer cells and cell clusters in the bone marrow, showing (**C**) the distance of the cancer cells to the cortical bone surface and (**D**) the size of cancer cells and clusters. (**E**) Volumetric quantification of breast cancer cell clusters on the periosteum. (**F**) Graphical 3D visualization of the distance of cancer cells in the bone marrow to the endocortical bone surface with the color code indicating the distance. (Asterisks in A.3 and A.4 indicate the presence of cancer cells and scale bars correspond to 500 µm (A and B) and 200 µm (A.1 – A.4) respectively. The box plots show the mean (C and D) or median (E) and first and third quartile. N = 5 bones from five tumor animals, representative images from one animal with a trabecular lesion.)

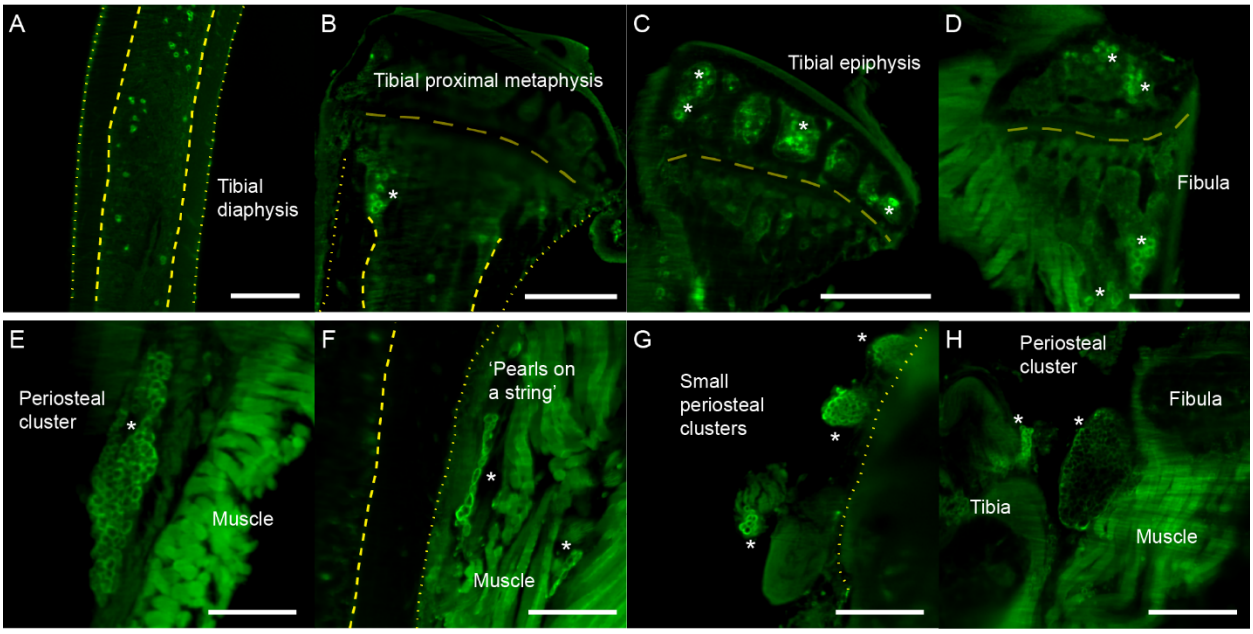

Fig. 2: LSFM visualization of cancer cells and cell clusters in various compartments of skeletal tissue.

Images showing cancer cells in the (**A**) tibial diaphysis, (**B**) tibial proximal metaphysis, (**C**) tibial epiphysis and (**D**) fibula, as well as in the periosteal tissue as (**E**) a large cluster, (**F**) like 'pearls on a string', (**G**) as small clusters and (**H**) as a large cluster between tibia and fibula. (Scale bars correspond to 500 µm (A-D) and 250 µm (E-F), cancer cells and patches are marked with an asterisk, while periosteal and endocortical bone, as well as the growth plate are marked with yellow lines. N = 5 bones from five animals.)

Location and growth of metastatic lesions in cortical bone detected by a new image analysis tool for pathological eroded bone patches

Overall bone (re)modeling can be studied and visualized by overlapping a reference scan (4 days prior to cancer cell injection) with later time points. This leads to three separate categories of bone: 1) constant bone (shown in yellow), 2) newly mineralized bone (shown in blue) and 3) eroded bone (shown in red), which can also be quantified in volume, surface and apposition/resorption rate.

To detect the location and track the growth of osteolytic lesions in cortical bone with microCT-based time-lapse morphometry data, a new image analysis tool was established that has the ability to differentiate between physiological and pathological erosion patches. The method is based on empirically determined threshold parameters to define a 3D neighborhood summing up eroded voxels as shown in Fig. 3A. Briefly, a first noise filtering is performed and only eroded bone patches are considered, which fulfill the criterion that 70% of the neighborhood (respectively 3 voxels in positive and negative x-, y- and z-direction) consists of erosion voxels (Fig. 3B). Next, to distinguish physiological vs. pathological erosion patches, we search for the pathological eroded bone patch core, which fulfills the harder criterion that 92.61% of a larger neighborhood (respectively 9 voxels in positive and negative x-, y-direction, 4 voxels in positive and negative z-direction) consists of eroded voxels (Fig. 3C). Finally, the volume of the pathological eroded bone patch is determined by the noise filtered patch including the eroded bone patch core (Fig. 3D). The threshold settings were obtained and validated with datasets from healthy control animals with physiological bone (re)modeling and no pathological eroded bone patches were detected.

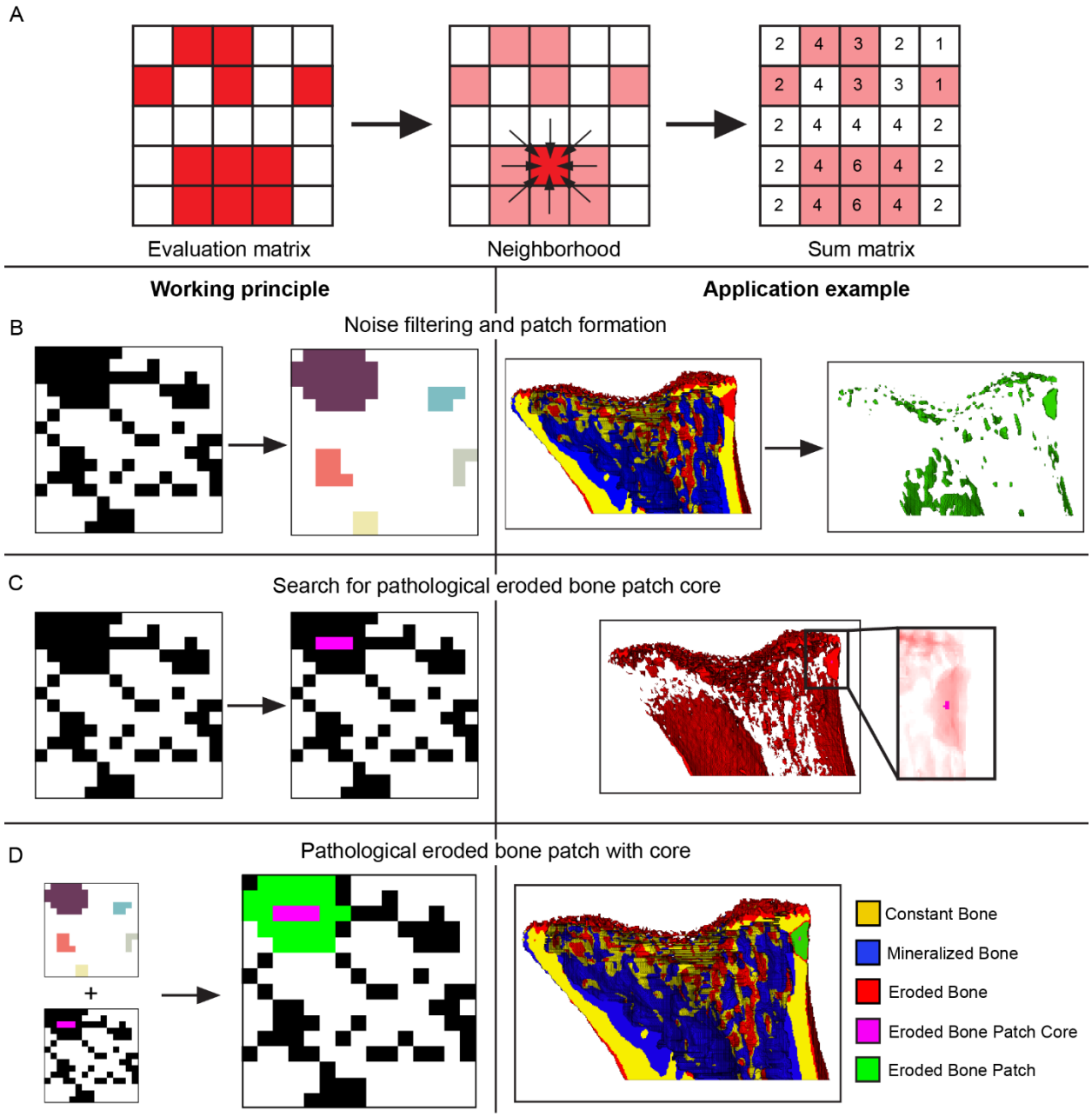

Fig. 3: Image analysis tool for pathological eroded bone patches using microCT-based time-lapse morphometry to detect the onset of metastatic bone lesions.

(**A**) Schematic showing how the neighborhood is determined, starting at the evaluation matrix, with a 2D simplified 3×3 neighborhood for one voxel and the resulting sum matrix for all voxels. Working principle (left) and application example (right) of the eroded bone patch analysis starting (**B**) the filtering of noise to form separate patches, (**C**) the search for a pathological

eroded bone patch core and (**D**) determining the volume of the eroded bone patch by identifying the filtered patch with the core. Constant bone is shown in yellow, mineralized bone in blue, eroded bone in red, eroded bone patch core in pink and eroded bone patch in green.

Osteolytic erosion patches were found in the cortical bone of six animals, with three in the tibia and three in the femur as shown in Fig. 4 and one exemplary osteolytic lesion in Supplementary Movies 3 and Movie 4. Five of these lesions started in the periosteum (Fig. 4A, B, D) and one in the endocortical region (Fig. 4C). All lesions were detected on day 17, which is the first time point that was measured after the reference scan (day 0, four days prior to cancer cell injection). The patch size at first detection varied between 0.005 – 0.025 mm^3, with equal distribution of smaller and bigger lesions in both femur and tibia. Lesions were tracked for up to 27 days (animals had to be sacrificed due to humane endpoint criteria) and in several animals the osteolytic eroded bone patch volume increased, with animal 1 starting at 0.01 mm^3 and reaching a final lesion size of nearly 0.1 mm^3 (Fig. 4E).

The eroded bone patch analysis enables the spatio-temporal visualization and quantification of osteolytic lesions, which improves the understanding of the onset of metastatic lesions. Several animals (Fig. 4A, B and D) exhibit first osteolytic lesions on the periosteal bone surface, suggesting an onset in that region.

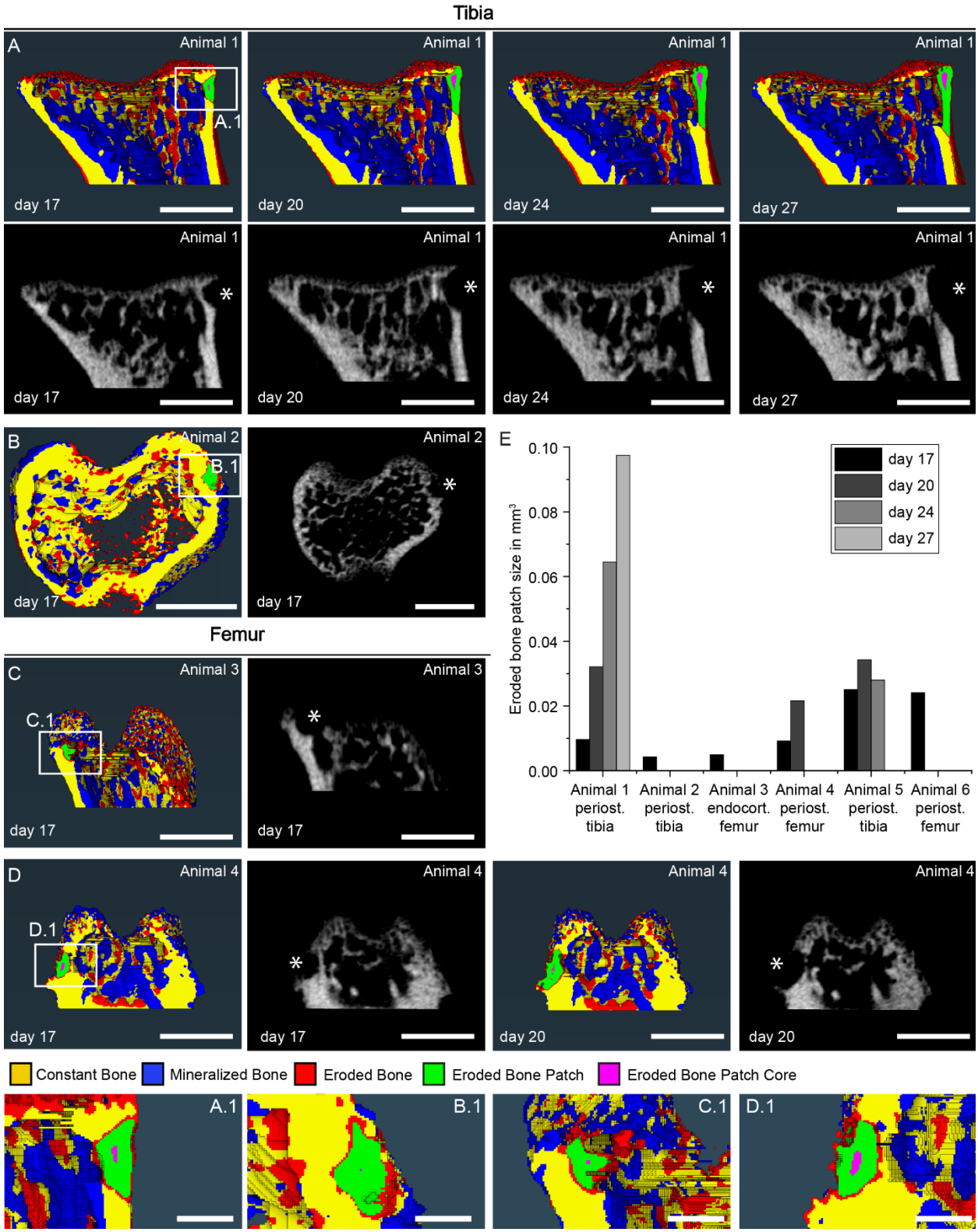
Tibia
A
Animal 1
A.1
day 17
day 20
day 24
day 27
B
Animal 2
B.1
Femur
C
Animal 3
C.1
D
Animal 4
D.1
E
Eroded bone patch size in mm³
0.10
0.08
0.06
0.04
0.02
0.00
day 17
day 20
day 24
day 27
Animal 1 periost. tibia
Animal 2 periost. tibia
Animal 3 endocort. femur
Animal 4 periost. femur
Animal 5 periost. tibia
Animal 6 periost. femur
Constant Bone
Mineralized Bone
Eroded Bone
Eroded Bone Patch
Eroded Bone Patch Core

Fig 4: **Spatio-temporal analysis of the location and growth of early metastatic lesions in cortical bone using microCT-based time-lapse morphometry and the new eroded bone patch image analysis tool**

Results of bone (re)modeling and detection of erosion-patches with constant bone in yellow, mineralized bone in blue, eroded bone in red, eroded bone patches in green and eroded bone patch core in pink are visualized for the (**A**) tibia of animal 1 at day 17 (with an enlargement in (**A.1**)), day 20, day 24 and day 27, with respective gray scale images shown below; (**B**) tibia of animal 2 at day 17 (with an enlargement in (**B.1**)) with the respective gray scale image. (Re)modeling analysis visualization for the (**C**) femur of animal 3 at day 17 (with an enlargement in (**C.1**)) with the respective gray scale and (**D**) femur of animal 4 at day 17 (with an enlargement in **D.1**) and day 20, with the respective gray scale images. (**E**) Quantitative results of the eroded bone patch analysis per animal up to 27 days. (Scale bars correspond to 1 mm, scale bar for enlargements 0.2 mm. The lesions are indicated with an asterisk in the gray scale images. N = 6 bones from six tumor animals.)

Metastatic lesions in trabecular bone have their onset directly on the mineralized surface adjacent to the growth plate

Metastatic osteolytic lesions in trabecular bone were visually detected in the primary spongiosa, right on the mineralized surface adjacent to the growth plate, both in the tibia (Fig. 5A-C) and femur (Fig. 5D). For all lesions, a top view and enlargements of a cross section are shown, both as bone (re)modeling analysis data and the respective gray scale image. The enlarged images (Fig. 5A.1-D.1) confirm that the growth plate is eroded in a larger area, spanning both along the growth plate and towards the secondary spongiosa. Although all lesions are still at a very early stage, Fig. 5B.1 clearly shows the smallest lesion with a diameter along the growth plate of under 200 µm. Two of the lesions are right between the condyles (Fig. 5A and D), the others do not show any distinct pattern.

To summarize, we were able to identify the onset of metastatic bone lesions visualized with microCT time-lapse morphometry, on both cortical and trabecular bone. Based on the location where they initiate, we identify: (i) fully cortical lesions that start on the periosteal side and do not attack the trabecular bone even after growing for 10 days (Fig. 4A); (ii) mixed lesions where both the endocortical bone (Fig. 4C)

and adjacent trabecular bone are resorbed (Fig. 5D); (iii) fully trabecular lesions located directly at the mineralized growth plate (Fig. 5).

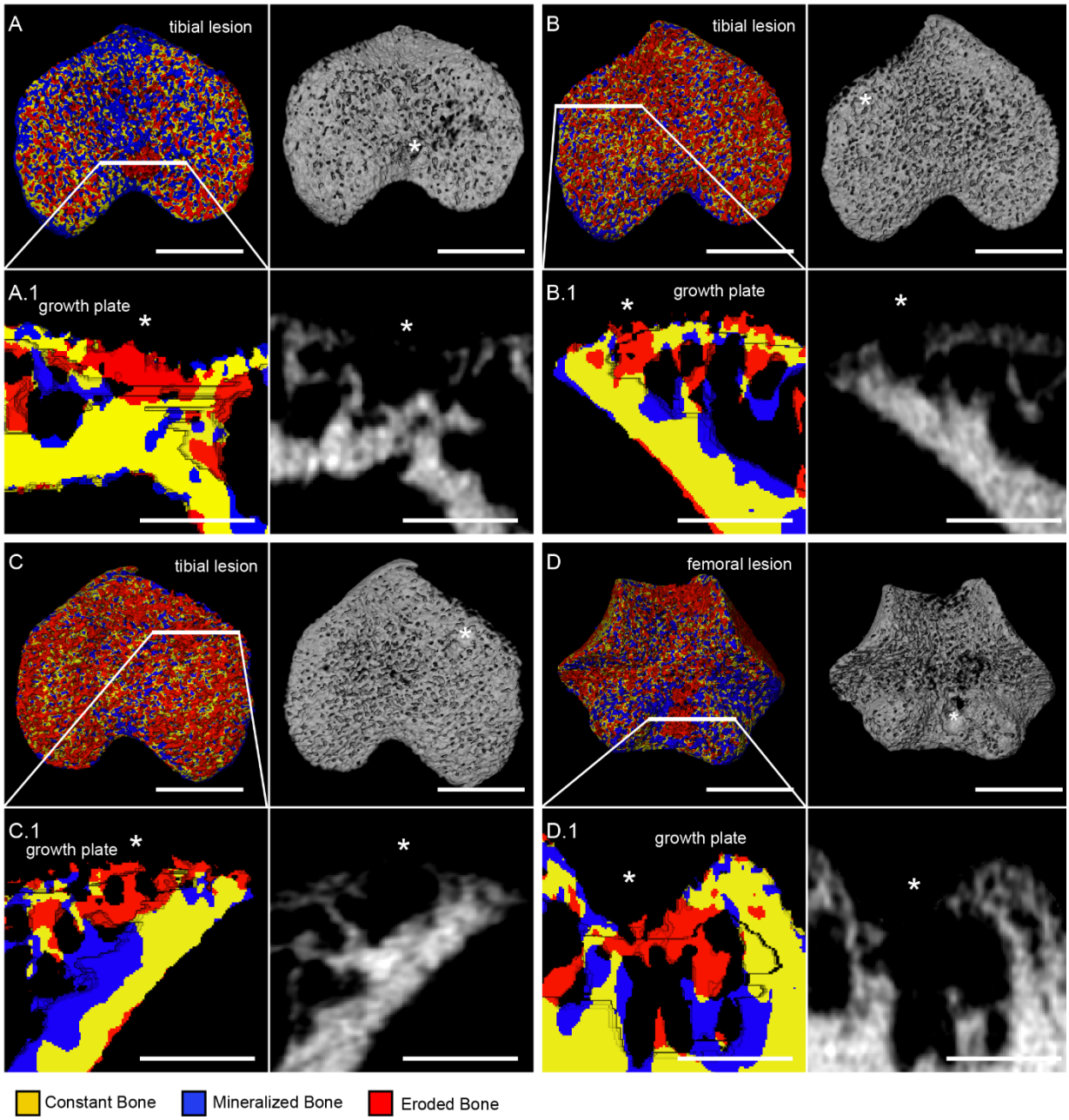

Fig. 5: Early metastatic lesions in trabecular bone of the primary spongiosa in femur and tibia using microCT-based time-lapse morphometry

Results of bone (re)modeling with constant bone in yellow, mineralized bone in blue, eroded bone in red, as well as gray scale images for bones at day 17. (**A**) (Re)modeling visualization top view, with respective gray scale image and (**A.1**) enlargement of

the cross-section of the osteolytic lesion for the left tibia of animal 1. (**B**) (Re)modeling visualization top view, with respective gray scale image and (**B.1**) enlargement of the cross-section for the left tibia of animal 2. (**C**) (Re)modeling visualization top view, with respective gray scale image and (**C.1**) enlargement of the cross-section for the right tibia of animal 2. (**D**) (Re)modeling visualization top view, with respective gray scale image and (**D.1**) enlargement of the cross-section for the right femur of animal 2. (Scale bars correspond to 1 mm and 0.5 mm for enlargements. The lesions are indicated with an asterisk. N = 4 bones from two tumor animals.)

Structural microenvironment of early metastatic bone lesions visualized with multiscale correlative tissue characterization

The early metastatic bone lesions detected with microCT-based time-lapse morphometry were then subjected to multiscale correlative tissue characterization to evaluate the structural microenvironment. Cortical and trabecular bone osteolytic lesions in femur (Fig. 6A-I) and tibia (Fig. 6J-R) were analyzed and compared with intact regions within the same bone. An overview image of the femur using backscattered electron (BSE) microscopy is shown in Fig. 6A, with the mineralized tissue of the bone being intact except for the cortical lesion in the posterior metaphysis (enlargement in Fig. 6B). The cortical bone is resorbed across nearly the entire cortical thickness, with only a thin layer remaining on the endocortical side. In the progression of such a small osteolytic lesion, the entire lacunae and canaliculi network is resorbed (Fig. 6C). The collagen analysis with second-harmonic generation (SHG) imaging also shows that all fibrillar collagen type I fibers that were part of the cortical bone have been resorbed (Fig. 6D). Interestingly, the thick collagen layer in the periosteum is still intact (Fig. 6D). The lesion region is now filled with a completely new soft tissue, with high density of cells larger than most cells found in other regions of the bone (Fig. 6E).

An overview image of the tibia using BSE microscopy is shown in Fig. 6J, with the mineralized tissue of the bone being intact except for the trabecular lesion on the anterior growth plate (enlargement in Fig. 6K). The mineralized part of the growth plate is visibly thinned out in that region and the surrounding trabeculae show a rough surface, indicating an ongoing erosion of the tissue. In analogy to

the cortical lesion, lacunae or canaliculi (Fig. 6L) and collagen fibers (Fig. 6M) are fully resorbed, while the growth plate on the posterior side (Fig. 6O-R) is fully intact. In summary, in both early cortical and trabecular lesions, the mineralized tissue, embedded lacunae and canaliculi, as well as collagen fibers within mineralized tissue are all fully resorbed and replaced by a new soft tissue with high density of cells larger than those normally found in the bone marrow or periosteal tissue.

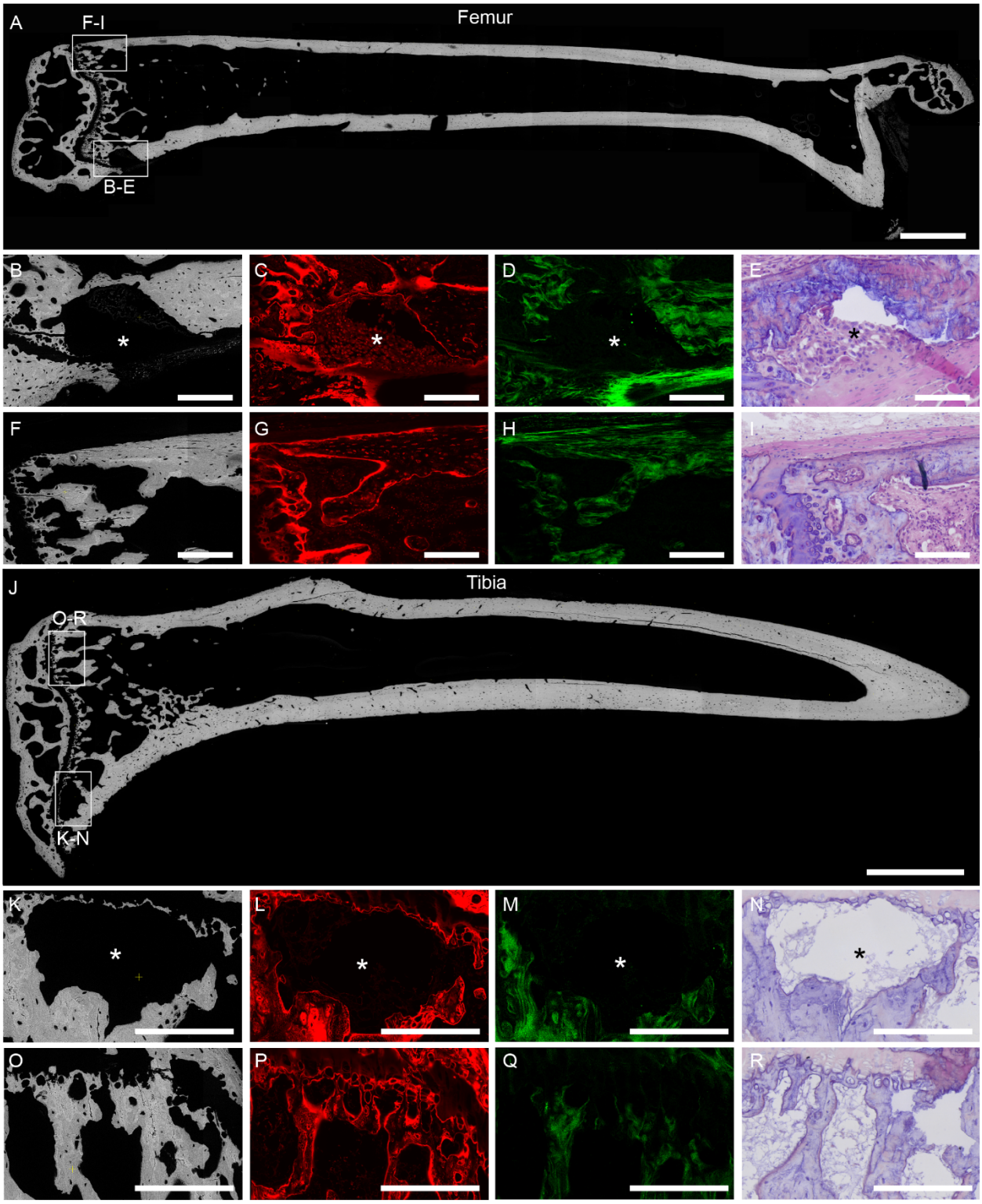

Fig. 6: Multiscale correlative tissue characterization of early metastatic lesions in cortical and trabecular bone and comparison with intact bone tissue in the same sample.

(**A**) Overview BSE microscopy image of a femur with (**B**) enlargement of a cortical lesion, as well as (**C**) CLSM of rhodamine-stained tissue, (**D**) SHG imaging of collagen fibers and (**E**) H&E stain. (**F**) BSE microscopy enlargement of an intact bone region, as well as (**G**) CLSM of rhodamine-staining tissue, (**H**) SHG imaging of collagen fibers and (**I**) H&E stain.
(**J**) Overview BSE microscopy image of a tibia with (**K**) enlargement of a trabecular lesion, as well as (**L**) CLSM (rhodamine staining), (**M**) SHG imaging of collagen fibers and (**N**) H&E stain. (**O**) BSE microscopy enlargement of a healthy trabecular region, as well as (**P**) CLSM (rhodamine staining), (**Q**) SHG imaging of collagen fibers and (**R**) H&E stain. (Asterisks indicate the presence of a lesion, scale bars correspond to 1 mm and 200 µm in the enlargements. N = 5 bones from five tumor animals containing an osteolytic lesion, representative images from two animals.)

Cancer cells in the bone marrow have a tendency for low proliferation

The proliferation state of the cancer cells and cell clusters in the bone marrow was analyzed using the proliferation marker Ki67. Sections from three bones harvested from three tumor animals, presenting with an osteolytic lesion in at least one bone, were imaged. In total 364 cells or clusters were detected in the bone marrow and analyzed for the proliferation status. Results are shown in Fig. 7A (with enlargements in A.1, and A.2) and quantification in Fig. 7B. For all bones a distinct area with a large number of cancer cells was analyzed which was either the metaphyseal or upper diaphyseal region. A cluster of cells was counted as Ki67+ as soon as one cell in this cluster presented with a signal. High resolution examples of Ki67+ (Fig. 7A.1) and Ki67- (Fig. 7.2) are shown with single channel views in Fig. S1. It was shown that half of the cell clusters present with no Ki67- signal, while most others would only entail one cell with a positive signal.

Cancer cells can be found in close proximity to and inside of blood vessels

The distance of cancer cells and clusters in the bone marrow to blood vessels was analyzed using a staining for endothelial cells (CD31). Sections from four bones harvested from four tumor animals, with an osteolytic lesion in at least one hind limb were analyzed. Most cancer cells can be found in direct contact with blood vessels, only few at further distance with a maximum distance at 16 µm (Fig. 7C). Fig. 7D shows many cells also have an up to 100% overlap with blood vessels, visualized in Fig. 7E.1. In

addition, cancer cells can be found close to the endocortical bone surface, which is also a highly vascularized region (Fig. 7E.4).

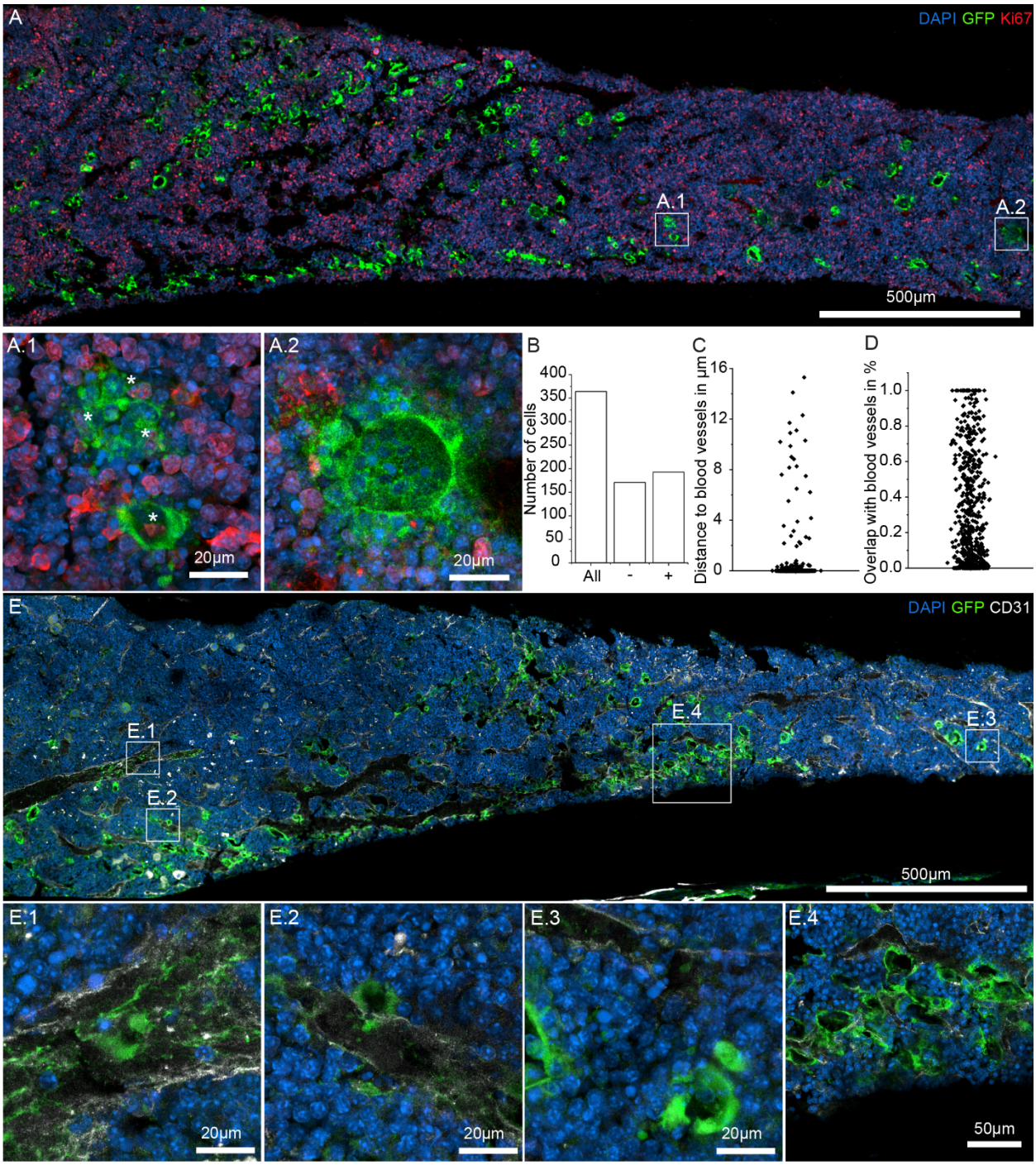

Fig. 7: Cancer cells and clusters are low in proliferation and home close to blood vessels.

Results of CLSM shown for (**A**) Ki67 proliferation marker with enlargement (**A.1**) showing Ki67 positive cell cluster and (**A.2**) showing Ki67 negative cell clusters. (**B**) Quantification of the Ki67 signal for all n = 364 analyzed cells. (**C**) Quantification of the distance of cancer cells and clusters to blood vessels and (**D**) quantification of the overlap of cancer cells with blood vessels. Results of CLSM shown for (**E**) CD31 with enlargement (E.1) showing cancer cell clusters inside a blood vessel, (E.2) showing a cancer cell cluster in direct contact with a blood vessel, (E.3) showing cancer cell clusters with a larger distance from blood vessels and (E.4) cancer cell clusters close to the endosteal bone surface. (Scale bars correspond to 500 µm and 20 µm for the enlargements, except for E.4 with 50 µm. DAPI staining of the nucleus in blue, eGFP of the cancer cells in green, Ki67 in red and CD31 in white. N = 3 bones (Ki67) from three tumor animals and N = 4 bones (CD31) from four tumor animals with osteolytic lesions in other long bones.)

Enhanced new mineralization in the absence of detectable osteolytic lesions

To study the systemic effects of cancer cells the bone (re)modeling of animals injected with cancer cells, but without detectable osteolytic lesions (n = 5), was studied for up to 38 days and compared with healthy animals injected with PBS (n = 7). The trabecular bone (re)modeling in the tibia proximal metaphysis is shown in Fig. 8A-H. An exemplary image of a tumor animal is depicted in Fig. 8A, the healthy PBS control animal in Fig. 8B, mineralization volume (MV/BV), surface (MS/BC) and mineral apposition rate (MAR) in Fig. 8C-E and erosion volume (EV/BV), surface (ES/BS) and mineral resorption rate (MRR) in Fig. 7F-H. The tumor animal shows more newly mineralized bone and less eroded trabeculae (Fig. 8A), in contrast with the healthy PBS animal, which shows both newly mineralized and eroded trabeculae (Fig. 8B). Higher MV/BV is observed for tumor animals at all time points (except for day 17, Fig. 8C), with values reaching between up to 1.5 – 2.5 for tumor animals, while it stays below 1 for healthy PBS animals, showing significant differences after day 31. Similar results are observed for MS/BS (Fig. 8D), while the MAR is only significantly elevated at day 38 (Fig 8E). Lower erosion in the tumor animals can be observed with EV/BV (Fig 8F), ES/BS (Fig. 8G), showing significant differences after day 34, and MRR (Fig. 8H) with significantly lower values at day 17, 20, 31, 34 and 38.

Analogous analysis is performed on the trabecular bone in the femur distal metaphysis (Fig. 8I-P). Volume, surfaces and apposition/resorption rate are shown in Fig. 8K-P, with the depiction of exemplary images for the tumor animals in Fig. 8I and healthy PBS animals in Fig. 8J. Similar trends as in the tibia are found in the femur, although the femur shows overall less (re)modeling and in the cortical bone (Fig. S2).

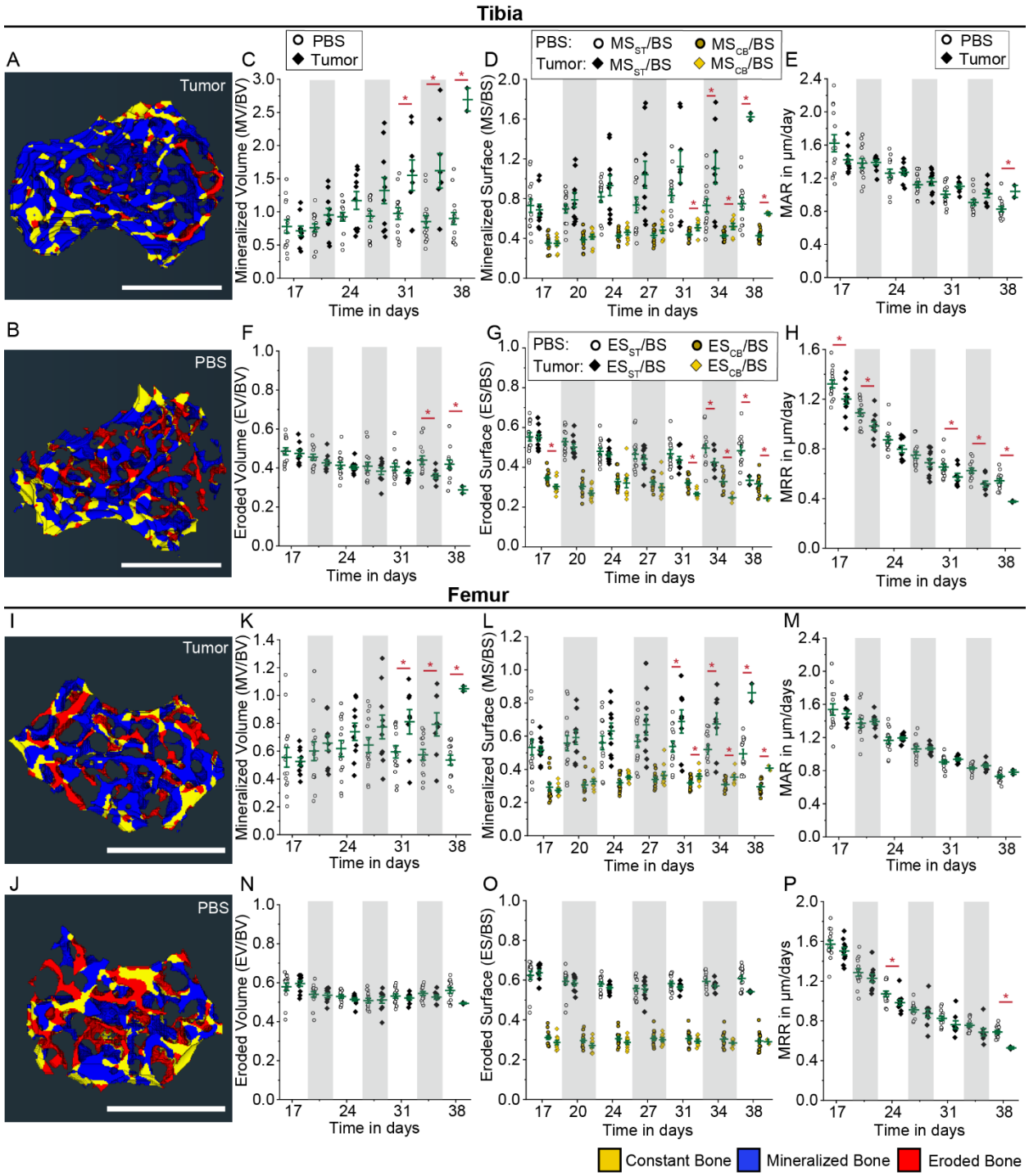

Fig. 8: Trabecular bone (re)modeling analysis of animals injected with cancer cells (without detectable osteolytic lesions) in comparison to healthy control animals in trabecular bone.

Results in trabecular bone of tibial proximal metaphysis are depicted for (**A**) tumor cell injected animals and (**B**) healthy PBS animals, with newly mineralized bone in blue, eroded bone in red and constant bone in yellow. Results are shown for (**C**) MV/BV, (**D**) MS_{ST}/BS as well as MS_{CB}/BS and (**E**) MAR, as well as (**F**) EV/BV, (**G**) ES_{ST}/BS as well as ES_{CB}/BS and (**H**) MRR. Results of bone (re)modeling analysis in trabecular bone of the femoral distal metaphysis depicted for (**I**) tumor cell injected animals and (**J**) healthy PBS animals, with newly mineralized bone in blue, eroded bone in red and constant bone in yellow. Results are shown for (**K**) MV/BV, (**L**) MS_{ST}/BS as well as MS_{CB}/BS and (**M**) MAR, as well as (**N**) EV/BV, (**O**) ES_{ST}/BS as well as ES_{CB}/BS and (**P**) MRR. (All plots show mean and standard deviation, with statistically significant values presented as * $p \geq 0.05$, a two sample t-tests was used. Scale bars correspond to 1 mm and exemplary images were taken from overlap data of day 34. PBS group: N = 14 bones from seven animals, Tumor group: N = 10 bones from five animals, for tibia and femur respectively.)

3. Discussion

We used multiscale and multidimensional methods *in vivo* and *ex vivo* to characterize the homing of cancer cells and the following onset of small osteolytic lesions, as well as bone (re)modeling in the absence of lesions of skeletally mature 12-week-old female BALB/c nude mice. The different dynamics in homing of cancer cells in both the periosteum and endosteum and the ability to establish cortical and trabecular lesions were shown for the long bones (tibia and femur), while altered bone (re)modeling with higher mineralization was detected in animals without osteolytic lesions. The combination of our methods allows a characterization of the dynamic bone tissue in the presence of cancer cells and small osteolytic lesions.

We studied the homing and localization of cancer cells and cell clusters for the first time in the intact 3D bone marrow, having the full spatial information, allowing the analysis of roughly 8,000 cells. The question of localization of cancer cells in the bone had been previously addressed in much detail using 2D sections, studying different types of niches. Carlson et al. came to the conclusion that cancer cells home in the perivascular niche, by analyzing the co-localization of the cells to blood vessels, osteoblasts and megakaryocytes[21]. Wang et al. on the other hand used immunological staining of RUNX2 and Osterix to

show that cancer cells were in direct contact with cells expressing these factors and hence finding them to be in the osteogenic niche[22]. Our findings align with both studies as the endocortical bone is both highly vascularized[16] and subject to high levels of mineralization in the tibia[20], giving rise to an overlap of the endocortical and perivascular niche. Additional analysis of the intact niche using our method in combination with further stainings could shed light on the highly debated question of the preferred cancer cell niche.

In our work, we show for the first time that already two weeks post-injection cancer cells can be found in different long bones (femur, tibia and fibula) and in all bone compartments including the epiphysis, metaphysis and diaphysis. This is specifically interesting in light of our *in vivo* microCT-based study. We clearly described a preference for osteolytic lesions to form in highly (re)modeled areas, like the primary spongiosa. In addition, no lesion was detected in the epiphysis or the diaphysis (visual control), leaving the metaphysis as the preferred site. Therefore, the ability for the cancer cells to reach certain locations is not sufficient as an explanation for the formation of osteolytic lesions, but calls for a new time dependent and dynamic criteria for a metastasis enhancing niche. This rather strengthens the hypothesis of antimetastatic niches as recently postulated for the skeletal muscle and parts of the bone marrow, describing inhospitable microenvironments where metastases rarely occur, if ever. Tumor cells are able to disseminate to these sites, but cannot colonize them in a meaningful timeframe, leading to the term ’antimetastatic’[23].

The eGFP+ breast cancer cells that we were able to detect using LSFM and CLSM form small tight clusters in the bone marrow and appear as small and large clusters in the periosteum with a volume of up to 0.1 mm^3. This might indicate that only small clusters or single cells can traverse capillaries and home in the bone marrow. In addition, the large clusters in the periosteum could be a sign of a more advanced stage of metastasis and are well in line with the osteolytic lesions we find in our microCT analysis, starting at the periosteum. The ability of cancer cells to form clusters has been described in the past and it was shown that clusters have a higher potential to survive and form lesions than single CTCs[24]. In this

work we show for the first time the localization and size of cancer cell clusters with 3D imaging of (intact) bones using LSFM. The results lead to the hypothesis that lesions are only formed if cancer cells are able to spread to a certain area and the dynamic (re)modeling of the bone tissue enhances the growth of the lesion in that area.

In this work we have presented a new image analysis tool to detect and track the evolution of early osteolytic lesions, with initial sizes as small as 0.004 mm^3. The eroded bone patch analysis helped us to reliably find cortical osteolytic lesions as early as two weeks after cancer cell injection (with the first time point measured). The tool was tested with healthy PBS injected animals for up to six weeks post injection, to rule-out the detection of non-pathological erosion patches. A similar tool was developed in the past by Campbell et al., where a distance transformation was used to detect the osteolytic lesions[25] with a lowest distance of 150 µm for all planes (in x, y and z), omitting the specific characteristic of osteolytic lesions to grow across the cortical thickness (in x and y). In addition, the published tool was not tested on healthy mice that undergo major (re)modeling especially at early ages (before 12 weeks). Our eroded bone patch analysis has proven reliable in finding early osteolytic lesions without detecting physiological eroded bone patches. With the help of this eroded bone patch analysis tool we were able to detect two different kinds of osteolytic lesions in the cortical bone. The majority of cortical lesions in this study were either located or initiated at the periosteal side (n = 5 out of 6). This type of cortical lesion had not been much reported in the past, but we found it to be the most frequent form of lesion in our entire study. The second type of cortical lesion found in this study was an endocortical lesion with trabecular involvement, as both cortical and trabecular bone get eroded[20].

Next to cortical lesions, we analyzed very early lesions in the trabecular bone. All of the lesions were visually detected two weeks after the cancer cell injection and were located at the growth plate area, eroding the mineralized primary spongiosa (n = 4). The growth plate is one of the most (re)modeled areas within the bone and further supports the idea that (re)modeling could be a driver for metastasis. Previous studies have also found that younger mice that undergo high bone (re)modeling suffer from more

metastases than older animals after intracardiac injection, even if the same number of cells arrive at the bone[18]. To overcome this, we used skeletally mature 12-week-old mice, but the local (re)modeling that is present in animals of all ages could be a driver for metastasis. Overall, osteolytic lesions were detected in cortical and trabecular bone of the metaphysis, a region that undergoes more (re)modeling than the diaphysis[26] or the epiphysis[20], in both the trabecular bone and the cortical bone surface. With this we could show that the localization of lesions is highly specific, while the homing of cells is possible in all regions. Further studies with patient data could show if the observation of trabecular lesions starting at the growth plate and a higher rate of lesions in the metaphysis also holds true in human disease, which might help to advance screening by localizing early events at specific areas.

In this study, trabecular lesions were detected visually with the help of both original microCT images and microCT-based time-lapse morphometry, which might also lead to an underestimation of trabecular lesions in this study. The results we have shown here and the techniques established for cortical bone are promising for further efforts to develop tools that can (semi)automatically detect osteolytic lesions in trabecular bone, which is undergoing more (re)modeling and shows an overall less dense structure.

With the help of our powerful *in vivo* microCT-based eroded bone patch analysis tool we were able to detect osteolytic lesions two weeks after the cancer cells had been injected. At this point the lesions were still small and in a very early phase. In addition, we used the microCT-based time-lapse morphometry visualization to detect osteolytic lesions in trabecular bone at the same early time point. With our *ex vivo* multimodal analysis, we have studied different parts of the metastatic cortical and trabecular lesions, with focus on the mineralized tissue and collagen fibers. Here we show the ex vivo analysis for a cortical lesion starting at the periosteum and a trabecular lesion close to the growth plate, with the BSE microscopy images confirming the microCT findings in both cases. Previous work focusing on the mineralized tissue has shown animals with massive lesions, 4-6 weeks after injection, where much of the mineralized tissue had already been eroded and, hence, no clear localization and trace of the onset of the lesion could be made[11]. With the help of rhodamine staining and CLSM, as well as SHG imaging, we

were able to show that even in small lesions, the collagen fibers and the entire mineralized tissue were resorbed. This means that important structures of the canaliculi network were dramatically disrupted, especially in the case of cortical lesions spanning the entire cortical thickness. The canaliculi network plays an important role in the mechano-sensitivity of the bone through fluid flow patterns[27]. The disruption of these patterns and the apoptosis of osteocytes could in return change the 'biophysical sensitivity' of larger bone areas. In addition, the network architecture could get hijacked by cancer cells for long distance signaling to other bone parts, as they have been shown to get in direct contact with osteocytes[28].

Next to the niche itself we also studied the cells found in the bone marrow. High proliferation is a sign for an outgrowing metastasis, often stained for with the proliferation marker Ki67. Miller et al. showed in the past that the absence of Ki67 is a clear signal that a cell is in G0/G1 phase[29]. Therefore, Ki67 is an important indicator to show if metastatic cell clusters are already highly proliferative. We found that only half of the cell clusters analyzed had at least one signal for Ki67+ and could therefore be categorized as active. This further enhances the theory that the bone marrow can be both metastatic and antimetastatic[23], as cancer cell clusters were found in the entire bone marrow but lesions only in specific areas.

In addition, cancer cell clusters were found to be located close to and within blood vessels, with only few cells positioned further away. The perivascular niche has been described as both activating and dormancy inducing[21,30], while a second hypothesis places cancer cells in the endocortical niche, following the mechanisms of HSCs[31]. Our work clearly shows that cancer cells and clusters are located both close to blood vessels and the endosteal bone surface, but as the cortical bone is also highly vascularized by trans-cortical vessels[16] the two different niches might not be in conflict with each other.

Next to animals with osteolytic lesions, we studied the altered (re)modeling in animals with cancer cell injection, but without visible osteolytic lesions for up to nearly five weeks post injection, investigating the systemic effect of circulating tumor cells or established metastases in other regions on the (re)modeling in long bones. Trabecular bone in both femur and tibia showed increased mineralization in volume and

surface, with significant differences compared to control animals detectable at later time points (31 days onward). The differences were more pronounced in the tibia, which is more (re)modeled in the physiological state compared to the femur. In addition, we found that the erosion is slightly down regulated in the tibia, shown in the volume and surface parameters, but specifically in the MRR. These findings show a clearly different trend compared to animals with large osteolytic disease as described in the literature[19].

These findings cause a controversy in the field and we speculate about two possible mechanisms behind this increase in mineralization and partial reduction in erosion. It could be a mechanism by breast cancer cells from the primary tumor or other secondary sites to prepare the premetastatic niche and increase the chances of establishing metastasis at later time points. In this context, Chiou et al. had shown a similar trend of more mineralized bone in animals injected with tumor conditioned media, suggesting that the increased mineralization is not caused by direct cancer cell contact and could precede osteolytic disease caused by metastasis[8]. For prostate cancer cells, accompanied by osteoblastic bone disease, it has been shown that their homing is supported by an osteoblast-rich niche[32], a hypothesis postulated for breast cancer but not yet proven. As an alternative mechanism, it has been suggested that the increased mineralization might be a reaction to prevent the homing and proliferation of cancer cells, creating an antimetastatic niche. It has been reported that cancer cells secrete factors that expand the osteoblast population, leading to ’educated’ osteoblasts, which cause tumor cell suppression and p21 upregulation in tumor cells[33]. Currently, it is not known which tumor derived factors are responsible for the changes in osteoblast activity[34] and the only well established path is the stimulation of RANKL expression by parathyroid hormone-related protein (PTHrP)[35,36]. Brown et al. had shown though, that the location of tumor cells is crucial for the fate of bone cells, as cancer-induced changes in osteoblast and osteoclast numbers differed substantially depending on whether or not the bone cells were in direct contact with tumor cells. In particular, in areas not in direct contact with tumor cells, they showed increased numbers

of osteoblasts and reduced numbers of osteoclasts compared to controls, which aligns with our findings as it would lead to more mineralization[34].

In summary we were able to show that cancer cells home in all bone compartments using intact bones, with a preference for small clusters in the bone marrow and larger clusters in the periosteum. Osteolytic lesions on the other hand were only detected in the metaphysis and we were able to identify three different types of lesions: 1) cortical lesions initiating in the periosteum, 2) cortical lesions initiating in the endocortical bone with trabecular erosion and 3) trabecular lesions in the primary spongiosa. These findings support the hypothesis that dynamic bone (re)modeling is a driver for metastasis and gives cancer cells the ability to establish an osteolytic disease. A multiscale characterization of early lesions showed that not only the mineral but also the collagen fibers are fully resorbed, causing severe changes in the LCN. The cellular analysis revealed that half of the cancer cells and clusters are non-proliferative and home close or even within blood vessels. We were further able to show that bone (re)modeling is altered in the absence of visible osteolytic lesions, leading to higher mineralization which could either speak for a pre- or antimetastatic niche and presenting a dynamic change as a result of systemic cancer cells. Our work gives important 3D and dynamic information and new perspectives on homing of cancer cells and the establishment of small osteolytic lesions in the long bones.

4. Materials and Methods

4.1 Animal model

12-week-old female BALB/c nude mice (CAnN.Cg-Foxn1nu/Crl, Charles River, Sulzfeld, Germany) were received and acclimatized in the animal facility of the Charité - Universitätsmedizin Berlin. The mice were housed 2-4 animals per cage with ad libitum access to food and water. A reference microCT scan was acquired at day 0 and mice were injected after 4 days, under ultrasound guidance (Vevo2100, FUJIFILM VisualSonics Inc., Canada), into the left ventricle of the heart (one injection per mouse) using a 27G needle (Fig. S3A). The control mice (n=10) were injected with PBS to ensure compatibility after this stressful procedure, with 3 animals being sacrified at day 17 for better comparison within *ex vivo*

experiments, keeping the age of the animals and the exposure to radiation of the microCT as similar as possible. The tumor animals (n = 11) were injected with MDA-MB-231-1833 BoM cells ($5x10^5$ in 100 µL ice cold PBS). The animals received Carprofen (CP-Pharma Handelsgesellschaft mbH, Burgdorf, Germany) and Buprenorphin (CP-Pharma Handelsgesellschaft mbH, Burgdorf, Germany) as analgesic drugs while under anesthesia. During longitudinal *in vivo* imaging and the intracardiac injection animals were anesthetized using isoflurane (CP-Pharma Handelsgesellschaft mbH, Burgdorf, Germany) at 1-2% with oxygen as a carrier and the eyes were protected from drying with Pan-Ophtal gel (Dr. Winzer Pharma GmbH, Berlin, Germany). The initial average animal weight was 19.7 g ± 1.7 g for control animals and 20.3 g ± 1.9 g for tumor animals. The weight at sacrifice for the mice sacrificed after 45 days was 19.6 g ± 2.1 g and 19.5 g ± 0.6 g for the animals sacrificed after 17 days. The weight at sacrifice for the tumor animals at the respective days between day 17 and 38 was 19.2 g ± 2.0 g. All animal experiments were carried out according to the policies and procedures approved by local legal research animal welfare representatives (LAGeSo Berlin, G0224/18).

4.2 Cell culture

MDA-MB-231-1883 BoM cells were provided by Dr. Joan Massagué and purchased from the Antibody and Bioresource Core Facility of the Memorial Sloan Kettering Cancer Center, USA[37]. Briefly, MDA-MB-231 (ATCC ® HTB-26™) human epithelial breast cancer cells were stably transduced with a lentivirus expressing a triple-fusion reporter, forming MDA-MB-231 TGL cells[38]. The here used subclone 1833 is a bone tropic human cell line deriving from a metastasis formed by these MDA-MB-231 TGL cells hosted in a mouse. MDA-MB-231-1883 BoM cells were cultured in low glucose Dulbecco's Modified Eagle's Medium (DMEM) (Sigma-Aldrich, Taufkirchen, Germany) supplemented with 1% penicillin/streptomycin (Gibco) and 10% fetal bovine serum (FBS superior, Sigma-Aldrich, Taufkirchen, Germany). The cells were grown at 37 °C with 5% CO_2 and regular passaging.

4.3 Longitudinal *in vivo* microCT image acquisition

Longitudinal imaging of the hind limbs of the mice was performed with a high resolution microCT (U-CTHR, MILabs, Netherlands). The X-ray tube was operated at 50 kVp source voltage and 210 mA source current. Images were acquired at a step angle of 0.375° with 2 projections per step (75 ms exposure time), over a range of 360° and with 8.5 µm voxel size. Two aluminum filters with 100 µm and 400 µm thickness were used. The scan region included the entire femur and tibia of both hind limbs and was determined on an X-ray scout view. To prevent motion artifacts and ensure reproducibility, the anesthetized mice were positioned using an animal bed with the hindlimbs restrained. The scans were reconstructed using the MILabs Reconstruction software and a projection filter (Hann) was applied in the process to limit blurring. The scanner was calibrated before every scan using the internal calibration system. The animals were scanned with the microCT for a reference scan (day 0, 12-week-old). After 17 days, the animals were scanned twice per week up until maximum 45 days (on day 17, 20, 24, 27, 31, 34, 38, 41 and 45) (Fig. S3A). Anesthetized mice were sacrificed by cervical dislocation. The hind limbs were harvested and fixed with 4% paraformaldehyde (PFA) in PBS over night at 4 °C and stored in PBS until further processed.

4.4 Dynamic microCT-based time-lapse morphometry

The analysis was performed in accordance with Birkhold et al.[26,39] and Young et al.[20]. To assess morphological changes, microCT scans of each time point (day 17, 20, 24, 27, 31, 34, 38, 41 and 45) were compared to the reference scan at day 0, which ensures full information for all time points and no loss of events by changing the reference scan. We analyzed both limbs of all animals. The regions of interest (ROIs) were set at the distal femoral metaphysis and the proximal tibial metaphysis, reaching 10% of the bone length. Each region of interest (ROI) started at the end of the non-mineralized growth plate, on the interface where the primary spongiosa of the metaphysis is found, reaching towards the diaphysis. The ROI included both primary and secondary spongiosa of the metaphysis. The entire epiphysis and other connected bones were manually segmented from the metaphysis. The threshold to

remove the background was determined using the 3D Otsu-Method [40] (tool provided by the software Amira 2020.1, Thermo Fisher Scientific, MA, USA) and a list of all used thresholds is reported in the Supplementary Table S1 – S4 for healthy PBS animals and in Supplementary Table S5 – S8 for tumor animals.

The registration process and following evaluation was performed in accordance with Birkhold et al.[26] and Young et al.[20]. The images were pre-processed and aligned using Amira. During the pre-processing step, the dataset was pre-cropped to the respective ROI. The epiphysis and other connected bones such as the fibula were removed by manual segmentation.

For the registration process, later time point images were registered onto the reference image (day 0) using a 3D rigid registration algorithm. The threshold determined as described above was used to exclude background noise from the registration while keeping the grey scale of the respective bone region data set. A hierarchical strategy was chosen for the registration to avoid local minima, starting with coarse resampling and proceeding to finer resolutions under visual control to ensure correct registration. After the registration, the images were transformed into the same coordinate system using a Lanczos interpolation, keeping the voxel size constant. The images were then re-cropped according to the corresponding ROI.

Then the ROIs were segmented into trabecular and cortical bone using morphological operations as described by Birkhold et al.[26] and evaluated, both using custom-made MATLAB (MATLAB 2018a; The Mathworks, Inc. Natick, MA, USA) scripts (Fig. S3B). Bone morphological changes were evaluated as previously described: MV/BV (normalized parameters are divided by the respective bone volume or bone surface of the reference scan), normalized mineralized bone surface-to-soft tissue interface (MS_{ST}/BS), normalized mineralized bone surface-to-constant bone interface (MS_{CB}/BS), MAR (mean thickness of formed bone in µm/day), EV/BV, normalized eroded bone surface-to-soft tissue interface (ES_{ST}/BS) normalized eroded bone surface-to-constant bone interface (ES_{CB}/BS), as well as MRR (mean depth of resorbed bone in µm/days). Briefly, for each case only the concerning voxels, being labeled as constant,

mineralized or eroded voxels, were taken into consideration. The first layer of voxels was disregarded due to partial volume effects, leaving the second most outward layer of voxels to be considered as the soft tissue interface, while the constant bone interface was evaluated by expanding the constant bone surface by one voxel. For the surface evaluation only one layer of voxels was taken into account, while all voxels were counted for volume evaluations. The different interfaces giving rise to the four distinct surfaces were calculated independently of each other and can thus, in specific cases, contain the same voxels. The description of the surfaces is not influencing the analysis of volumetric parameters, which are calculated from all bone voxels independently. A list of all parameters with definition and unit is provided in Supplementary Table S9.

4.5 Reproducibility of image processing

The reproducibility of the registration and segmentation algorithm was determined in our previous study[20].

4.6 Osteolytic lesions in cortical bone: Eroded bone patch detection and volume analysis

To detect and analyze the volume of osteolytic lesions in cortical bone with dynamic microCT-based time-lapse morphometry data, a new image analysis tool was established that had the ability to differentiate between physiological erosion and pathological erosion patches in the cortical bone.

Only eroded voxels of previously segmented cortical bone were taken into account for this procedure. A chosen 3D neighborhood of each eroded voxel was evaluated, meaning that the status of surrounding voxels – being eroded or not eroded – and the voxel itself were considered and summed leading to a sum matrix. Two different empirically determined thresholds were applied to a) analyze the volume of the entire eroded bone patch and b) to detect the eroded bone patch core (the main criteria to determine whether or not an animal has a lesion)

To analyze the volume of the eroded bone patch, the noise in form of scattered eroded voxels around the eroded bone patch core was filtered: To do so, the neighborhood of each eroded voxel was explored in 3

voxels in positive and negative x-, y- and z-direction. If a threshold of 70% was fulfilled, those erosion voxels were maintained and contributed to the volume of the eroded bone patch. The threshold parameters were determined empirically under visual control. To detect the eroded bone patch core of only pathological erosions, the neighborhood of each eroded voxel was explored in 9 voxels in positive and negative x- and y-direction and in 4 voxels in positive and negative z-direction. If a threshold of 92.61% was fulfilled, meaning that 92.61% of the neighborhood voxels were erosion voxels, that voxel was identified as belonging to the eroded bone patch core. The parameters were determined empirically by testing visually detected lesions and data from healthy control animals. Only patches containing a core were quantified as pathological eroded bone patches.

The volume of each eroded bone patch in mm^3 was obtained at different time points. The location of osteolytic lesions was visualized with the eroded bone patch core shown in pink and the respective entire patch in green.

4.7 Lesion analysis in trabecular bone

Trabecular osteolytic lesions were detected visually both in the raw data and the microCT-based time-lapse morphometry data. An area was counted as a lesion if the mineralized part of the growth plate was fully resorbed, leaving a hole larger than normally visible in the spongy structure of the mineralized growth plate.

4.8 Code availability

The original code as well as the modified version used in this study are available on GitHub.

https://github.com/BWillieLab/Timelapse-Morphometry (original code)

https://github.com/CipitriaLab/Timelapse-Morphometry (modified code used in this and the previous study)

https://github.com/CipitriaLab/Timelapse-Morphometry/tree/lesion_analysis (patch analysis used in this study)

4.9 Statistical analysis

When comparing PBS controls with tumor animals, only bones harvested from animals without detectable osteolytic lesions in the hind limbs were included for the latter. All bones harvested from animals with confirmed lesions were excluded from microCT analysis. Both limbs of all animals were considered, resulting in seven control animals with n = 14 bones and 5 tumor animals with n = 10 bones. The plots show the mean and standard deviation. Two sample t-tests were used for statistical comparison between different groups and parameters with significant differences presented as * $p \leq 0.05$.

4.10 Optical clearing and light-sheet fluorescence microscopy of tibiae

Fixed tibiae were dehydrated in an ascending ethanol series (50, 70 and two times in 100%) for 12 h each at room temperature and cleared with ethyl cinnamate (Sigma-Aldrich, Taufkirchen, Germany) at room temperature for 24 h according to the simpleCLEAR protocol[16] (Fig. S3C).

To image cleared tibiae via LSFM, a LaVision BioTec Ultramicroscope Blaze (Miltenyi/LaVision BioTec, Bielefeld, Germany) with a supercontinuum white light laser (460 – 800 nm), 7 individual combinable excitation and emission filters covering 450 – 865 nm, an AndorNeo sCMOS Camera with a pixel size of 6.5 μm^3, and 1.1× (NA 0.1), 4× (NA 0.35), 12× (NA 0.53) objectives with a magnification changer ranging from 0.66× to 30× was used. For image acquisition, cleared samples were immersed in ethyl cinnamate in a quartz cuvette and excited at 470/30 nm for eGFP-excitation and 560/40 nm for tissue autofluorescence excitation. eGFP was detected using a 525/50 nm band-pass emission filter and a 620/60 nm band-pass emission filter was used for tissue autofluorescence detection. Because the excitation optics of the microscope provide a light-sheet thickness of 4 – 24 µm (adjustable NA), the Z-step size was set to 5 or 10 µm depending on the selected light-sheet NA. The optical zoom factor varied from 1.66× to 4× depending on the objectives and digital zoom factors used.

Imaris (Bitplane, Version 9.6.0, Oxford Instruments, Abingdon, UK) was used for data analysis. The bone marrow was segmented manually and the cells were analyzed using the spots tool with an initial estimated

diameter of 35.5 µm that was found by manually measuring around 10 cells. N = 5 bones from five different animals were analyzed.

The clearing protocol was reversed by placing samples in a descending ethanol series (100, 70, 50%) with 1% Tween-20 for 5 h at room temperature each, followed by two steps in PBS with 1% Tween-20 (5 h at room temperature each). The samples were stored in PBS until further usage.

4.11 Resin embedding of mineralized bone tissue and sectioning using controlled angle cutting and *ex vivo* microcomputed tomography

Bone specimens were cold embedded at 4 °C in poly(methyl methacrylate) (PMMA) (Technovit 9100, Kulzer, Germany), following the manufacturer's instructions. Briefly, samples were dehydrated in an ascending ethanol series rhodamine solution (4.17 mg/mL−1 Rhodamine B, pure in 100% ethanol, ACROS Organics, Geel, Belgium), followed by a xylene washing, pre-infiltration and infiltration, each for 48 h at 4 °C, and final embedding in PMMA.

In order to expose the metastatic osteolytic lesion, we used controlled angle cutting as described by Moreno-Jimenez et al.[41]. The excess PMMA was first trimmed and the entire block scanned with an *ex vivo* microCT scanner (EasyTom micro/nano tomograph RX solutions, France) at a low resolution with 15 µm voxel size and acquisition parameters of 107 kV, 93 µA, frame rate of 6 and average frame of 5. Reconstruction of the 800 projections/scan were performed using RX Solutions X-Act software. The cutting plane to capture the metastatic osteolytic lesion was found using Data Viewer (Bruker, Kontich, Belgium). For small correction angles under 20°, a tilted cylinder was cut and the sample blocks were fixed on it for sectioning. For larger correction angles over 20°, an additional cut of the block was performed with a diamond wire saw (DWS.100, Diamond WireTec GmbH & Co.KG, Weinheim, Germany) and a second microCT scan was performed, repeating the same procedure as above. The histological sections were taken at a thickness of 6 µm with a microtome (Leica RM2255 Microtome, Leica Biosystems, Wetzlar, Germany).

4.12 Haematoxylin and eosin staining

The PMMA embedded sections were stained using a standard protocol of haematoxylin and eosin (H&E) (H&E Rapid kit, Clin-Tech, Surrey, UK). In short, samples were rehydrated in a descending ethanol series, followed by staining in Carazzi's double-strength haematoxylin. After another wash in tap water, the slides were stained in eosin, rinsed in tap water, dehydrated in an ascending ethanol series (70, 80, 96, 100% twice for 2 min each), incubated in xylene twice for 2 min and mounted (VITROCLUD, deltalab, Barcelona, Spain). The stained sections were imaged with a Keyence Digital Microscope (VKX-5550E, Keyence, Germany). Mineralized tissue and nuclei are shown in dark purple, while soft tissue is shown in light purple.

4.13 Tartrate-resistant acid phosphatase staining

The PMMA embedded sections were stained using a standard protocol of tartrate-resistant acid phosphatase (TRAP) staining. In short, samples were rehydrated in a descending ethanol series. Samples were then incubated in TRAP buffer (sodium acetate 40 mM, VWR, Radnor, US, and disodium tartrate dihydrate 10mM, Merck KGaA, Darmstadt, Germany), followed by an incubation in pre-warmed TRAP staining solution (in TRAP buffer, naphthol AS-MXphosphate 0.2 mg/mL, Sigma-Aldrich, Taufkirchen, Germany, fast red violet LB salt 1.2 mg/mL, Sigma-Aldrich, Taufkirchen, Germany, N,N-dimethlyformamid 2%, Sigma-Aldrich, Taufkirchen, Germany and Triton X 1%, Thermo Fisher Scientific, Waltham, US) at 37 °C for 2 h under repeated visual control. The sections were counter stained with Mayer's haematoxylin (Sigma Aldrich, Taufkirchen, Germany). The Sections were incubated in aniline blue solution (aniline blue 0.4 mg/mL, phosphotungstic acid 12 mg/mL, Carl Roth, Karlsruhe, Germany), blotted to remove access liquid, followed by xylene incubation and mounted with mounting media (VITROCLUD, deltalab, Barcelona, Spain). The stained sections were imaged with a Keyence Digital Microscope (VKX-5550E, Keyence, Germany). Osteoclasts are shown in pink, nuclei in pale blue and bone tissue in blue.

4.14 Confocal laser scanning microscopy fluorescence imaging

After sectioning, the exposed PMMA block surface was polished (PM5, Logitech, Glasgow, Scotland) with abrasive paper 4000 with grading of 5 µm and with 3 µm and 1 µm diamond spray under constant visual control, ensuring that only minimal tissue got removed. The block surface of the rhodamine stained samples was imaged using CLSM (Leica TCS SP8 DLS, Multiphoton, Leica Microsystems CMS GmbH, Wetzlar, Germany). The samples were images with a HC PL APO CS2 40×/1.30 oil objective (NA 1.3) at a magnification of 40×. Argon laser light with $\lambda_{excitation}$ = 514 nm / $\lambda_{emission}$ = 550 – 650 nm was used with a laser intensity of 10%. Images were acquired with a resolution of 1024 pixels by 1024 pixels (pixel size of 284 nm) at a scan speed of 400 Hz. Over 100 images for each sample with a thickness of 347 nm, spanning a changing thickness of around 50 µm depth from the block surface were imaged. To compensate for the loss of signal during scanning along the depth, the photomultiplier gain was continuously increased. The images were stitched and visualized with the LAS X software (Version 3.5.7.23225, Leica Microsystems CMS GmbH, Wetzlar, Germany). For each animal, a region containing an osteolytic lesion, either in the cortical or trabecular bone, and a lesion-free region in the same bone at a comparable location were imaged. N = 5 bones from five different animals were analyzed.

4.15 Second harmonic generation imaging

SHG imaging was performed on the exact same ROI with the same instrument and objective. A pulsed infrared laser ($\lambda_{excitation}$ = 910 nm/ $\lambda_{emission}$ = 450 – 460 nm) with a power of 0.6 W and an intensity of 10% was used. Images were acquired with a resolution of 1024 pixels by 1024 pixels (pixel size of 284 nm) at a scan speed of 400 Hz. Around 20 images with a thickness of 2.758 µm were acquired, keeping the same total depth as for the previous image of rhodamine staining and fluorescence imaging. For each animal a region containing an osteolytic lesion, either in the cortical or trabecular bone, and a lesion-free region at a comparable location were imaged. The images were stitched and visualized with the LAS X software (Version 3.5.7.23225, Leica Microsystems CMS GmbH, Wetzlar, Germany). N = 5 bones from five different animals were analyzed.

4.16 Backscattered electron imaging

The polished PMMA block surface of the samples was imaged with an environmental scanning electron microscope (Quattro ESEM, Thermo Fisher Scientific, Waltham, US) in backscattered electron mode. The following settings were used: 15 kV, low vacuum conditions (100 Pa), working distance of approximately 8 mm, spot size of 3 and 500× magnification. The images were manually stitched using Adobe Photoshop 2022. N = 5 bones from five animals were analyzed.

4.17 Cryo-embedding and -sectioning of mineralized bone tissue

Bones of one limb of each mouse without a detectable osteolytic lesion were freeze embedded following the method of the SECTION-LAB Co. Ltd. (Hiroshima, Japan). Briefly, the samples were dehydrated in an ascending sucrose solution (10, 20 and 30% in distilled water) for 24 h each at 4 °C. Next, a metal mold was placed in isopropanol cooled with liquid nitrogen and filled with embedding medium (SCEM; SECTION-LAB Co. Ltd., Hiroshima, Japan). The bone was placed in the middle and covered with embedding medium, avoiding direct contact with the cooled isopropanol. Samples were stored at −80 °C until further usage. Cryosections with a thickness of 20 µm were cut following the Kawamoto method using a cryostat (Leica CM3060S, Leica Microsystems CMS GmbH, Wetzlar, Germany). The sections were collected using Kawamoto films (type 2C(9), SECTION-LAB Co. Ltd., Hiroshima, Japan), then attached to a microscopic slide and stored at -20 °C until further use.

4.18 Histological immunofluorescence staining and imaging

For IF staining the slides were blocked with blocking buffer (1%bovine serum albumin (BSA), Sigma-Aldrich, Taufkirchen, Germany, 0.1% Tween20 Carl Roth, Karlsruhe, Germany, 0.1% dimethyl sulfoxide (DMSO), Merck KGaA, Darmstadt, Germany in PBS) for 1 h. Primary and secondary antibodies were diluted in blocking buffer and incubated for at least 4 h at room temperature or over night at 4 °C, with in between washing steps (three times, 15 min each) in washing buffer (0.1% Tween20, 0.1% DMSO in PBS). Final washing steps were conducted in washing buffer (twice for 15 min) and in distilled water (once for 15 min). Slides were then mounted with Dako fluorescence mounting media (S302380-2,

Agilent Technologies, Santa Clara, US). The primary antibodies and respective concentrations used in this study are the following: 4',6-diamidino-2-phenylindole (DAPI) (1:500, Roche), anti-Ki67 (1:100, 14-5698-82, eBioscience™) and anti-CD31 (1:200, 102516, Biolegend). As secondary antibody Alexa Fluor 555 (1:1000, 4417S, Cell Signaling Technology) was used. Samples were imaged using CLSM (Leica TCS SP8 DLS, Multiphoton, Leica Microsystems CMS GmbH, Wetzlar, Germany).

Three different objectives were used: HC APO L 10x/0.30 water objective (NA 0.3) at a magnification of 10×, HC PL APO CS2 40×/1.30 oil objective (NA 1.3) at a magnification of 40×, HC PL APO CS2 63x/1.40 oil objective (NA 1.4) at a magnification of 63×. For imaging the DAPI, Diode 405 laser light with $\lambda_{excitation}$ = 405nm / $\lambda_{emission}$ = 410 – 483nm was used. For imaging the eGFP, argon laser light with $\lambda_{excitation}$ = 488nm / $\lambda_{emission}$ = 493 – 556nm was used. For imaging the Alexa Fluor 555, DPSS 561 laser light with $\lambda_{excitation}$ = 561nm / $\lambda_{emission}$ = 566 – 756nm laser light was used. For imaging the Alexa Fluor 647, HeNe 633 laser light with $\lambda_{excitation}$ = 633nm / $\lambda_{emission}$ = 638 – 755nm was used. Laser intensity and photomultiplier gain were kept constant: DAPI (intensity 1%, HyD detector, gain 30), eGFP (intensity 20%, Hyd SMD 2 detector, gain 2900), Alexa Fluor 555 (intensity 1%, PMT detector, gain 650) and Alexa Fluor 647 (intensity 3%, HyD detector, gain 200). Images were acquired with a resolution of 1024 pixels by 1024 pixels (pixel size of 284 nm) at a scan speed of 400 Hz (200 Hz for 63× magnification), and a varying number of images with a thickness of 4 µm (2 µm for 63× magnification) were made over a depth of around 20 µm. For 10× and 40× magnification, tile scans depending on the size of the sample were acquired.

Images were analyzed using Imaris (Imaris Viewer 9.8.0, Oxford Instruments, Abingdon, United Kingdom) with 40× magnification images being used for quantification, thresholds were applied manually under visual control. For Ki67 analysis, cells/clusters were manually segmented using the surface tool on each layer. Nuclear Ki67 signal was overlapped using the DAPI signal and counted automatically. For distance analysis with CD31, cancer cells were estimated on one layer using the surface tool. CD31 was segmented using the surface tool and distance mapping and overlapping were

calculated automatically. Images were visualized with Imaris. N =3 (Ki67) and N = 4 (CD31) bones from four animals were analyzed.

Acknowledgements:

This work was funded by the Deutsche Forschungsgemeinschaft (DFG) Emmy Noether grant (CI 203/2-1 to A. C., S. A. E. Y., and D. S. G.). A. C. also thanks the funding from IKERBASQUE Basque Foundation for Science and from the Spanish Ministry of Science and Innovation (PID2021-123013OB-I00). A.-D. H. thanks the International Max Planck Research School (IMPRS) on Multiscale Bio Systems for financial support. The FRQS Programme de bourse de chercheur provided support to B.W. We thank the lab of Dr. Joan Massagué at the Memorial Sloan Kettering Cancer Center, USA, for providing the MDA-MB-231-1883 BoM cells. We thank Jeannette Steffen for technical assistance with sectioning and staining. The authors would like to acknowledge Peter Fratzl, Sadra Bakhshandeh and Hubert Taieb for scientific discussion.

Conflict of interest:

The authors declare no conflict of interest

References

1. Torre, L. A. *et al.* Global cancer statistics, 2012. *CA. Cancer J. Clin.* **65**, 87–108 (2015).

2. Coleman, R. E. Clinical Features of Metastatic Bone Disease and Risk of Skeletal Morbidity. *Clin. Cancer Res.* **12**, 6243s-6249s (2006).

3. Weilbaecher, K. N., Guise, T. A. & McCauley, L. K. Cancer to bone: a fatal attraction. *Nat. Rev.*

Cancer **11**, 411–425 (2011).

4. Harbeck, N. *et al.* Breast cancer. *Nat. Rev. Dis. Prim.* **5**, 66 (2019).

5. Coleman, R. E. *et al.* Bone metastases. *Nat. Rev. Dis. Prim.* **6**, 83 (2020).

6. Phan, T. G. & Croucher, P. I. The dormant cancer cell life cycle. *Nat. Rev. Cancer* **20**, 398–411 (2020).

7. Croucher, P. I., McDonald, M. M. & Martin, T. J. Bone metastasis: the importance of the neighbourhood. *Nat. Rev. Cancer* **16**, 373–386 (2016).

8. Chiou, A. E. *et al.* Breast cancer–secreted factors perturb murine bone growth in regions prone to metastasis. *Sci. Adv.* **7**, 1–14 (2021).

9. Crist, S. B. & Ghajar, C. M. When a House Is Not a Home: A Survey of Antimetastatic Niches and Potential Mechanisms of Disseminated Tumor Cell Suppression. *Annu. Rev. Pathol. Mech. Dis.* **16**, 409–432 (2021).

10. Price, T. T. *et al.* Dormant breast cancer micrometastases reside in specific bone marrow niches that regulate their transit to and from bone. *Sci. Transl. Med.* **8**, 340ra73-340ra73 (2016).

11. He, F. *et al.* Multiscale characterization of the mineral phase at skeletal sites of breast cancer metastasis. *Proc. Natl. Acad. Sci.* **114**, 10542–10547 (2017).

12. Di Martino, J. S. *et al.* A tumor-derived type III collagen-rich ECM niche regulates tumor cell dormancy. *Nat. Cancer 2021* 1–18 (2021). doi:10.1038/s43018-021-00291-9

13. Fonta, C. M. *et al.* Fibronectin fibers are highly tensed in healthy organs in contrast to tumors and virus-infected lymph nodes. *Matrix Biol. Plus* **8**, 100046 (2020).

14. Choi, S. *et al.* Intrafibrillar, bone-mimetic collagen mineralization regulates breast cancer cell adhesion and migration. *Biomaterials* **198**, 95–106 (2019).

15. Grüneboom, A. *et al.* Next-generation imaging of the skeletal system and its blood supply. *Nat. Rev. Rheumatol.* **15**, 533–549 (2019).

16. Grüneboom, A. *et al.* A network of trans-cortical capillaries as mainstay for blood circulation in long bones. *Nat. Metab.* **1**, 236–250 (2019).

17. Fratzl, P. & Weinkamer, R. Nature's hierarchical materials. *Prog. Mater. Sci.* **52**, 1263–1334 (2007).

18. Wang, N. *et al.* The frequency of osteolytic bone metastasis is determined by conditions of the soil, not the number of seeds; evidence from in vivo models of breast and prostate cancer. *J. Exp. Clin. Cancer Res.* **34**, 124 (2015).

19. Johnson, L. C. *et al.* Longitudinal live animal micro-CT allows for quantitative analysis of tumor-induced bone destruction. *Bone* **48**, 141–151 (2011).

20. Young, S. A. E. *et al.* In vivo microCT-based time-lapse morphometry reveals anatomical site-specific differences in bone (re)modeling serving as baseline parameters to detect early pathological events. *Bone* **161**, 116432 (2022).

21. Carlson, P. *et al.* Targeting the perivascular niche sensitizes disseminated tumour cells to chemotherapy. *Nat. Cell Biol.* **21**, 238–250 (2019).

22. Wang, H. *et al.* The Osteogenic Niche Promotes Early-Stage Bone Colonization of Disseminated Breast Cancer Cells. *Cancer Cell* **27**, 193–210 (2015).

23. Crist, S. B. & Ghajar, C. M. When a House Is Not a Home: A Survey of Antimetastatic Niches and Potential Mechanisms of Disseminated Tumor Cell Suppression. *Annu. Rev. Pathol. Mech. Dis.* **16**, 409–432 (2021).

24. Aceto, N. *et al.* Circulating Tumor Cell Clusters Are Oligoclonal Precursors of Breast Cancer Metastasis. *Cell* **158**, 1110–1122 (2014).

25. Campbell, G. M. *et al.* Tracking the Progression of Osteolytic and Osteosclerotic Lesions in Mice Using Serial In Vivo μCT: Applications to the Assessment of Bisphosphonate Treatment Efficacy. *J. Bone Miner. Res.* **33**, 410–418 (2018).

26. Birkhold, A. I. *et al.* Mineralizing surface is the main target of mechanical stimulation independent of age: 3D dynamic in vivo morphometry. *Bone* **66**, 15–25 (2014).

27. van Tol, A. F. *et al.* Network architecture strongly influences the fluid flow pattern through the lacunocanalicular network in human osteons. *Biomech. Model. Mechanobiol.* (2019). doi:10.1007/s10237-019-01250-1

28. Hemmatian, H. *et al.* Reorganization of the osteocyte lacuno-canalicular network characteristics in tumor sites of an immunocompetent murine model of osteotropic cancers. *Bone* 116074 (2021). doi:10.1016/j.bone.2021.116074

29. Miller, I. *et al.* Ki67 is a Graded Rather than a Binary Marker of Proliferation versus Quiescence. *Cell Rep.* **24**, 1105-1112.e5 (2018).

30. Ghajar, C. M. *et al.* The perivascular niche regulates breast tumour dormancy. *Nat. Cell Biol.* **15**, 807–817 (2013).

31. Dhawan, A. *et al.* Breast cancer cells compete with hematopoietic stem and progenitor cells for intercellular adhesion molecule 1-mediated binding to the bone marrow microenvironment. *Carcinogenesis* **37**, 759–767 (2016).

32. Wang, N. *et al.* Prostate Cancer Cells Preferentially Home to Osteoblast-rich Areas in the Early Stages of Bone Metastasis: Evidence From In Vivo Models. *J. Bone Miner. Res.* **29**, 2688–2696 (2014).

33. Kolb, A. D., Shupp, A. B., Mukhopadhyay, D., Marini, F. C. & Bussard, K. M. Osteoblasts are "educated" by crosstalk with metastatic breast cancer cells in the bone tumor microenvironment.

Breast Cancer Res. **21**, 31 (2019).

34. Brown, H. K., Ottewell, P. D., Evans, C. A. & Holen, I. Location matters: osteoblast and osteoclast distribution is modified by the presence and proximity to breast cancer cells in vivo. *Clin. Exp. Metastasis* **29**, 927–938 (2012).

35. Mundy, G. R. Mechanisms of bone metastasis. *Cancer* **80**, 1546–1556 (1997).

36. Zarrer, J., Haider, M., Smit, D. J. & Taipaleenmäki, H. Pathological Crosstalk between Metastatic Breast Cancer Cells and the Bone Microenvironment. *Biomolecules* **10**, 337 (2020).

37. Minn, A. J. *et al.* Genes that mediate breast cancer metastasis to lung. *Nature* **436**, 518–524 (2005).

38. Ponomarev, V. *et al.* A novel triple-modality reporter gene for whole-body fluorescent, bioluminescent, and nuclear noninvasive imaging. *Eur. J. Nucl. Med. Mol. Imaging* **31**, 740–751 (2004).

39. Birkhold, A. I. *et al.* The influence of age on adaptive bone formation and bone resorption. *Biomaterials* **35**, 9290–9301 (2014).

40. Otsu, N. A Threshold Selection Method from Gray-Level Histograms. *IEEE Trans. Syst. Man. Cybern.* **9**, 62–66 (1979).

41. Moreno-Jiménez, I., Garske, D. S., Lahr, C. A., Hutmacher, D. W. & Cipitria, A. Targeted 2D histology and ultrastructural bone analysis based on 3D microCT anatomical locations. *MethodsX* **8**, 101480 (2021).